Localized spirals in Taylor-Couette flow

M. Heise, J. Abshagen, D. Küter, K. Hochstrate, and G. Pfister
Institute of Experimental and Applied Physics, University of Kiel, 24098 Kiel, Germany

Ch. Hoffmann
Institute of Theoretical Physics, Saarland University, 66041 Saarbrücken, Germany
(Received 28 September 2007; published 5 February 2008)

We present a type of spiral vortex state that appears from a supercritical Hopf bifurcation below the linear instability of circular Couette flow in a Taylor-Couette system with rigid end plates. These spirals have been found experimentally as well as numerically as "pure" states but also coexist with "classical" spirals (or axially standing waves for smaller systems) which typically appear from linear instability in counterrotating Taylor-Couette flow. These spiral states have an axial distribution of the strongly localized amplitude in the vicinity of the rigid end plates that confine the system in the axial direction. Furthermore, they show significantly different oscillation frequencies compared to the critical spiral frequencies. Despite the localization of the amplitude near the ends, the states appear as global states with spirals that propagate either toward the middle from each end of the system or vice versa. In contrast to classical spirals, these states exhibit a spatial or a spatiotemporal reflection symmetry.

DOI: 10.1103/PhysRevE.77.026202 PACS number(s): 05.45.−a, 47.20.Ky, 02.30.Oz

I. INTRODUCTION

One of the classical systems for the study of bifurcation events in hydrodynamics is Taylor-Couette flow [1–6]. It consists of a viscous fluid confined in the gap between two concentric, independently rotating cylinders. Under the assumption of infinite axial length, the basic laminar flow is circular Couette flow (CCF) which has a translational invariance and reflection symmetry in axial as well as a rotational invariance in the azimuthal direction. CCF is thus invariant under the group $O(2)\times SO(2)$ [6,7]. For sufficiently high rates of counterrotation, spiral vortices (SPI) occur in CCF via a symmetry-breaking Hopf bifurcation with O(2) symmetry as a result of a linear instability [8,9]. These spirals are traveling waves in axial and rotating waves in the azimuthal direction with an azimuthal wave number $m=\pm 1$ (for the parameter values considered here). Standing waves (SWs)—e.g., the superposition of two traveling waves—are also a possible solution arising from linear stability analysis [8].

Spiral vortices were found first theoretically by Krueger *et al.* [10] and experimentally by Snyder [11]. Systematic experimental as well as combined numerical and experimental studies on counterrotating Taylor-Couette flow have been carried out by Andereck *et al.* [12] and Langford *et al.* [9], respectively. These experimental studies have been performed for different radius ratios in systems with aspect ratios (e.g., the axial length scaled by the gap width) from 17 to 48. As the first time-dependent pattern that appears from basic flow, they observed spiral vortices for a wide range of counterrotation rates in agreement with numerical results from linear stability analysis. Numerical studies on spirals focusing on their nonlinear behavior have been performed by Sanchez *et al.* [13] and Hoffmann and Lücke [14].

Nonrotating end plates at top and bottom, as often used in experimental systems, subcritically induce axisymmetric Ekman vortices in the annulus—see, e.g., [15–17]. Spiral vortices then exist in a bulk region which is bound by rotating defects in the vicinity of the axisymmetric Ekman vortices near the end plates [18]. Considering the symmetry of such a flow of finite axial extent, it has been predicted theoretically by Crawford and Knobloch [19] and Landsberg and Knobloch [20] that oscillatory bifurcation with broken translational invariance differs from its counterpart in infinite systems. The influence of finite axial length on the transition to spirals has been theoretically investigated by adding symmetry-breaking terms to the normal form of a Hopf bifurcation with O(2) symmetry. Because of the broken translational invariance, two different types of SWs (denoted SW_0 and SW_π) appear supercritically instead of spiral vortices and have a purely spatial reflection symmetry or a spatiotemporal glide-reflection symmetry, respectively. Traveling-wave-type solutions, such as spiral vortices, arise exclusively super- or subcritically from a secondary steady bifurcation of the SW solutions. Experimental investigations on Taylor-Couette flow reveal such a difference in the bifurcation behavior for sufficiently small aspect ratios [21].

Here we report on a type of spiral vortices that appear axially localized near rigid end plates below the onset of spiral vortices or SWs. These flow states are ultimately related to variations of the basic flow in Taylor-Couette systems with rigid boundaries since they are not captured by linear stability analysis of CCF considering infinite axial length. Basic flow in Taylor-Couette systems with rigid boundaries differs from CCF due to the presence of so-called Ekman vortices accompanied by an inhomogeneous azimuthal flow.

II. EXPERIMENTAL SETUP AND NUMERICAL SIMULATION

The Reynolds number of the inner (i) and outer (o) cylinders serves as a control parameter, $\mathrm{Re}_{i,o}=dr_{i,o}\Omega_{i,o}/\nu$, where $\Omega_{i,o}$ denotes the angular velocity of the inner (i) and outer (o) cylinders, respectively. In our experimental Taylor-

Couette flow the temperature of the fluid is thermostatically controlled to (24.00 ± 0.01) °C. Silicone oil with a kinematic viscosity $\nu = 10.6$ cS is used as working fluid. The inner cylinder of the apparatus is machined from stainless steel having a radius of $r_i = (12.50 \pm 0.01)$ mm, while the outer cylinder is made from optically polished glass with a radius of $r_o = (25.00 \pm 0.01)$ mm. The flow is confined in the axial direction by two end plates having a distance L which defines the axial length of the system. Geometric parameters are the aspect ratio $\Gamma = L/d$, with gap width $d = r_o - r_i$ and radius ratio $\eta = r_i/r_o$. In this study the radius ratio is held fixed at $\eta = 0.5$ and most of the measurements have been performed at $\Gamma = 8$. We utilize laser Doppler velocimetry (LDV) for measurements of the local flow velocity. All LDV measurements are recorded at a radial distance of 1 mm from the inner cylinder. In addition to that, flow visualization measurements are performed in order to distinguish between different flow states because of their spatiotemporal patterns.

The flow is described by the Navier-Stokes equations (NSEs) for incompressible fluids. Using cylindrical coordinates, we decompose the velocity field $\mathbf{u} = v_r \mathbf{e}_r + v_\varphi \mathbf{e}_\varphi + v_z \mathbf{e}_z$ into a radial component v_r, an azimuthal one v_φ, and an axial one v_z. For numerical calculations, we used a combined Galerkin and finite-difference code in the axial and radial directions. We used homogeneous grids with discretization lengths $\Delta r = \Delta z = 0.05$ which have shown to be more accurate than nonhomogeneous grids. In the azimuthal direction eight Fourier modes are used. Since we are studying finite-length cylinders with end plates bounding the annulus vertically, we do not use a spectral decomposition in the axial direction for numerical simulations. At the axial end plates, finite boundary conditions were imposed by rigid, nonrotating lids. The grids for the velocity fields are chosen in a way that they do not fall together with discontinuities in the corners (see [18] for further details).

In addition to the above-described numerical method linear stability thresholds were obtained by a shooting algorithm using a fourth-order Runge-Kutta integration with a discretization of $\Delta r = 0.005d$ in radial direction and a Fourier decomposition in the axial direction. This numerical method is used in order to represent Taylor-Couette flow with infinite axial length (see [22] for further details).

III. MEASUREMENT TECHNIQUE

In Fig. 1(a) an axial scan of the axial velocity v_z recorded at $\mathrm{Re}_o = -120.0$ and $\mathrm{Re}_i = 117.5$ is depicted. In this measurement the axial position $z(t) = v_{\mathrm{LDV}} t$ of the LDV is given by the scan velocity v_{LDV}. The axial scan has been performed experimentally by measuring the axial velocity of the flow while simultaneously moving the LDV in the axial direction from top to bottom at constant velocity, and each data point represents a distinct axial position $z(t)$. The axial scan presented here is referred to a SW, which is a result of a superposition of two spiral waves traveling in the opposite axial direction on the one hand and the underlying Ekman vortex structure on the other hand. SWs are typically observed in counterrotating Taylor-Couette flow with $\eta = 0.5$ for $\Gamma \lesssim 12$ [18,21,23,24].

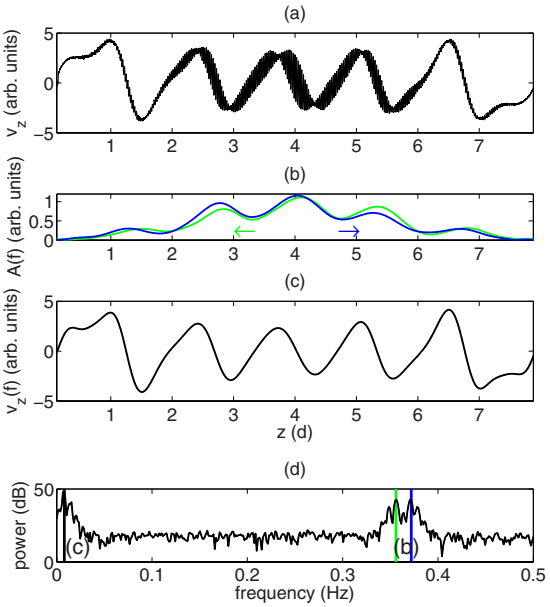

FIG. 1. (Color online) (a) Axial scan of the axial velocity v_z of a SW recorded at $\mathrm{Re}_o = -120.0$ and $\mathrm{Re}_i = 117.5$, (b) amplitudes $A(f)$ of SPI↓ [green (light gray) (0.340–0.365 Hz)] and SPI↑ [blue (dark gray) (0.365–0.390 Hz)], (c) bandpass-filtered scan of (a) (0–0.025 Hz), and (d) power spectrum of (a). The solid lines mark the corresponding frequencies in (b) and (c).

In addition to the typical Ekman vortex profile, an oscillation of the axial velocity v_z is observed in almost each axial position, but also nodal points are visible at some certain axial positions in the system. In these nodal points, the axial velocity v_z is constant and this is a strong indicator of SWs.

In Fig. 1(d) the corresponding power spectrum of (a) is shown. The three solid lines indicate the relevant frequency peaks of the spiral vortices [blue (dark gray) and green (light gray)] and the Ekman vortices (black). Due to the way an axial scan of the axial velocity is performed, two frequency peaks are observed: one for each spiral. As a result of a Doppler shift, one peak corresponds to the upward- SPI↑ [blue (dark gray) line] and the other to the downward- [green (light gray) line] traveling spiral SPI↓. For the first one, the axial motion of the LDV is in the opposite direction to the spiral motion, whereas it is in the same direction for the latter. Note that both frequencies are identical for the case of a stationary LDV measurement in any position of the system [14,25]. By applying a narrow bandpass filter it is possible to separate these three different flow states from each other. The result of such a bandpass filtering of the axial scan in Fig. 1(a) for the frequencies which correspond to the Ekman vortex structure (0–0.025 Hz) is displayed in (c). By comparing this with the original signal in (a) one recognizes the underlying Ekman structure. Note that the Ekman vortices are stationary and the corresponding frequency peak in (d) simply reflects the axial motion of the LDV.

In Fig. 1(b) the amplitudes of the upward- [blue (dark gray) line] and downward- [green (light gray) line] propagating spirals (SPI↓ and SPI↑) are shown. These amplitudes $A(f)$ are an estimate of the envelope of the bandpass-filtered axial scan. The axial propagation directions of both spirals

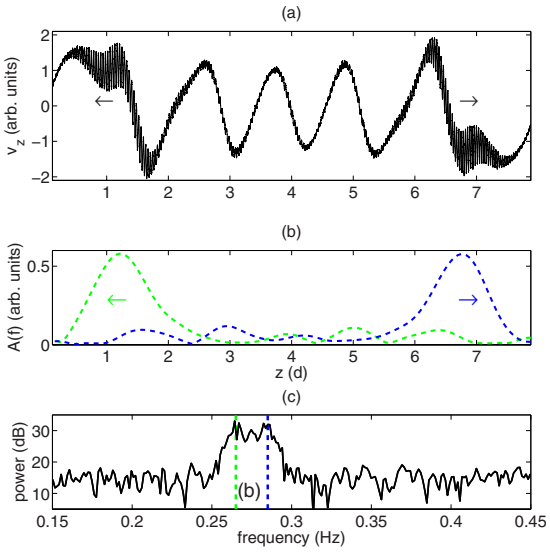

FIG. 2. (Color online) (a) Axial scan of the axial velocity v_z of SPI_+ recorded at $Re_o=-156.0$ and $Re_i=129.0$, (b) amplitudes $A(f)$ of downward-propagating SPI_+ [green (light gray) (0.255–0.275 Hz)] and upward-directed SPI_+ [blue (dark gray) dashed line (0.275–0.295 Hz)], and (c) power spectrum of (a). The dashed lines mark the corresponding frequencies in (b).

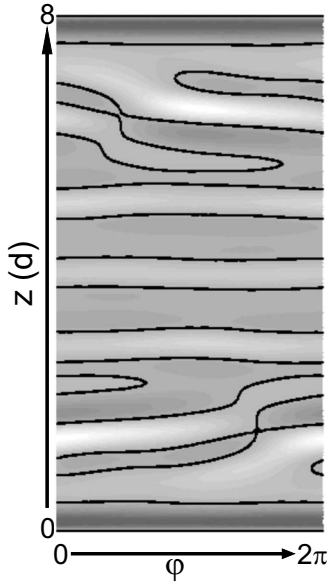

FIG. 3. Numerically calculated visualization of the radial velocity $v_r(\varphi,z)$ of SPI_+ in axial and azimuthal directions at the midgap at $Re_o=-156.0$ and $Re_i=129.0$. The left-handed spiral structure is located at the upper part and the right-handed one at the lower part of the system.

are indicated by the (colored) arrows in (b). Apart from the decay of the spiral amplitude in the vicinity of the end plates, both spiral amplitudes are almost uniformly distributed over the whole bulk of the system as is expected for SWs.

In the following, the measurement technique presented above is used to study these spiral states and to separate the different types of traveling waves from each other. Note that the underlying Ekman structure will not be shown in the following since it does not differ qualitatively for all flow states presented here.

IV. RESULTS

A. Localized spirals SPI_+

In Fig. 2(a) an axial scan recorded at $Re_o=-156.0$ and $Re_i=129.0$ is depicted. In addition to the underlying Ekman vortex structure, oscillations which are localized near the end plates are visible. The oscillation frequencies can be seen in the corresponding power spectrum depicted in Fig. 2(c) and are indicated by a green (light gray) and blue (dark gray) dashed line.

As exemplarily shown in Sec. III for SWs, a single-frequency peak in a stationary LDV measurement is split up into two peaks in the axial scans because of a Doppler shift. The peak marked with the blue (dark gray) dashed line corresponds to a wave that travels upwards, whereas the green (light gray) dashed line corresponds to a downward traveling one. A bandpass filter allows one to distinguish both traveling waves from each other as well as from the Ekman vortex profile. The amplitude of each spiral (separated by bandpass filtering) is shown in Fig. 2(b) with the bandpass frequencies for the upward- [blue (dark gray), 0.275–0.295 Hz] and downward- [green (light gray), 0.255–0.275 Hz] propagating waves. Two (colored) arrows in (b) additionally indicate the axial propagation direction. The amplitude of the upward-traveling spiral is dominant near the upper whereas the amplitude of the downward-traveling spiral is dominant near the lower end plate. Flow visualization measurements have shown that these waves are spiral vortices rotating in the azimuthal direction and propagating in the axial direction.

The spiral structure of SPI_+ is also verified by numerical simulations of the NSEs. Figure 3 gives the numerically calculated radial velocity $u(\varphi,z)$ in the (φ,z) plane at midgap for $Re_o=-156.0$ and $Re_i=129.0$. The left-handed spiral structure at the upper part and the right-handed one at the lower part of the system is visible. In addition to that the toroidal closed vortex structure of the flow is visible in the bulk of the system. The numerically determined oscillation frequency ($f_{num}=0.28$ Hz) is in good agreement with the experimental one ($f_{expt}=0.26$ Hz).

We call this localized spiral state SPI_+ because of the phase generation near the axial middle of the system (indicated by +) and propagation toward the end plates. Therefore, this flow state breaks the rotational invariance, but still has a spatiotemporal reflection symmetry as shown in Fig. 3. The oscillation frequency of this flow state in numerical simulation, $f_{num}=0.28$ Hz, and in experiment, $f_{expt}=0.26$ Hz, is below the one predicted by linear stability analysis of CCF, $f_{stab}=0.44$ Hz, for the parameters considered here ($Re_o=-156$ and $\nu=10.6$ cS. The wavelength of this flow state, $\lambda_{num}=1.40d$, is above the one predicted by the linear instability of CCF, $\lambda_{stab}=1.32d$.

B. Localized spirals SPI_-

In Fig. 4(a), an axial scan recorded at $Re_o=-200.0$ and $Re_i=140.1$ is depicted. Similar to the scan displayed in Fig.

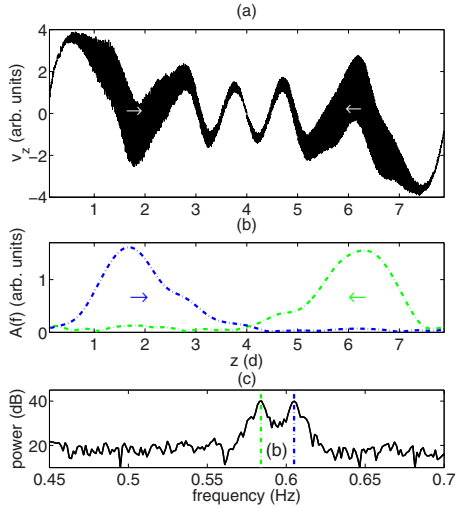

FIG. 4. (Color online) (a) Axial scan of the axial velocity v_z of SPI_ recorded at $\mathrm{Re}_o=-200.0$ and $\mathrm{Re}_i=140.1$, (b) amplitudes of downward-propagating SPI_ [green (light gray) (0.575–0.595 Hz)] and upward-propagating SPI_ [blue (dark gray) dash-dotted line (0.595–0.615 Hz)], and (c) power spectrum of (a). The dash-dotted lines mark the bandpass-filtered frequencies in (b).

FIG. 5. Numerically calculated visualization of the radial velocity $v_r(\varphi,z)$ of SPI_ in axial and azimuthal directions at the midgap at $\mathrm{Re}_o=-200.0$ and $\mathrm{Re}_i=137.0$.

2(a), the Ekman vortex structure and a localized oscillation near each end boundary are observed.

In the corresponding power spectrum in Fig. 4(c), a double peak (caused by the Doppler shift) is visible. The peak marked by the blue (dark gray) dash-dotted line corresponds to an upward-traveling wave, whereas the green (light gray) one corresponds to a downward-traveling one.

The corresponding amplitudes $A(f)$, determined by bandpass filtering the axial scan in (a), are shown in Fig. 4(b) for the bandpass frequencies of the upward- [blue (dark gray), 0.595–0.615 Hz] and downward- [green (light gray) dash-dotted line, 0.575–0.595 Hz] propagating spiral. The two (colored) arrows in (b) additionally indicate the axial propagation of the spirals.

Analog to the localized spirals SPI_+, the spiral structure of this flow state is verified by flow visualization experiments as well as by numerical simulations of the NSE. A numerical visualization of the radial velocity $u(\varphi,z)$ at midgap is depicted in Fig. 5. The parameters of this simulation are $\mathrm{Re}_o=-200.0$ and $\mathrm{Re}_i=137.0$, and the strong localization of the spiral structure in the flow at the upper and lower parts of the system is obvious.

In contrast to the localized spirals SPI_+, these spirals travel toward the axial middle. Due to the phase annihilation in the axial middle (indicated by the −), this localized spiral type is named SPI_. This flow state also breaks the rotational invariance, but still has a purely spatial reflection symmetry. The oscillation frequency in numerical simulation, $f_{\mathrm{num}}=0.595$ Hz, and in experiment, $f_{\mathrm{expt}}=0.58$ Hz, lies below the one predicted by linear stability analysis of CCF, $f_{\mathrm{stab}}=0.497$ Hz, for the parameters considered here ($\mathrm{Re}_o=-200$ and $\nu=10.6$ cS). The wavelength of this flow state, $\lambda_{\mathrm{num}}=1.10d$, is below the one predicted by linear instability of CCF, $\lambda_{\mathrm{stab}}=1.19d$. These spirals are right handed in the upper and left handed in the lower part of the system. The numerically determined oscillation frequency $f_{\mathrm{num}}=0.595$ Hz is also in very good agreement with the experimental one ($f_{\mathrm{expt}}=0.58$ Hz).

C. Bifurcation behavior of SPI_+

Localized spirals SPI_+ appear directly in the basic laminar flow even below the onset of spiral vortices. In order to characterize the transition toward localized spirals SPI_+, the square of the oscillation amplitude and the oscillation frequency are plotted as a function of Re_i in Fig. 6. The amplitude is estimated from the square of the mean value of the oscillation minima $\langle v_{z,\mathrm{min}}\rangle^2$ obtained from this flow state. The diagram depicted in Fig. 6 was recorded for $\mathrm{Re}_o=-156.0$ at an axial $h=19.8$ mm and radial position $r=r_i+1$ mm, where the axial velocity of the underlying basic flow is zero. A linear fit (solid line) of the squared amplitude verifies a square-root dependence of the amplitude as it is characteristic for Hopf bifurcations. The oscillation appears at $\mathrm{Re}_{i,c}=128.7$ (dashed vertical line) with an (nonvanishing) oscillation frequency of 0.28 Hz and is almost constant with Re_i. The frequency corresponds to SPI_+ (see Fig. 2), and therefore strong experimental evidence is provided in Fig. 6 that SPI_+ appears in basic flow from a Hopf bifurcation.

An investigation of the transient dynamics close to a bifurcation provides further information about the properties of this bifurcation. The critical slowing down—i.e., the divergence of time constants τ as the control parameter approaches the critical point $\mathrm{Re}_{i,c}$—is a typical dynamical phenomenon that occurs close to a supercritical Hopf bifurcation. Critical slowing down at Hopf bifurcations has been observed in Taylor-Couette flow [26] and at the onset of oscillations in magnetoconvection [27]. The method for extracting time constants from experimental time series is given in [26,28]. The experimentally determined time con-

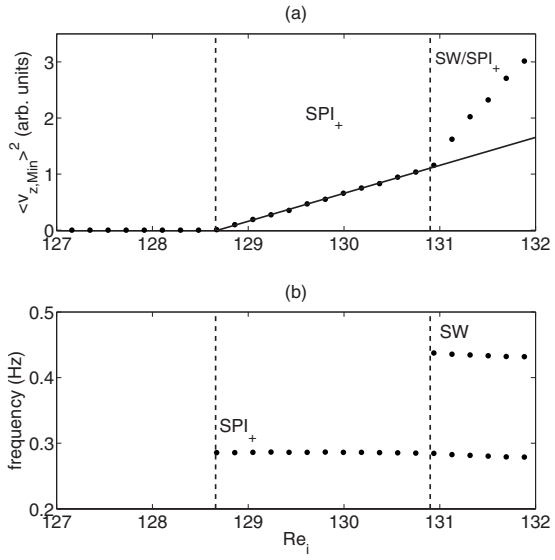

FIG. 6. Experimental bifurcation diagram recorded at $\mathrm{Re}_o=-156.0$ and axial $h=19.8$ mm and radial position $r=r_i+1$ mm. (a) Square of the mean value of the minima $\langle v_{z,\min}\rangle^2$ versus Re_i and (b) corresponding oscillation frequencies versus Re_i of localized spirals SPI_+ and SWs. The dashed lines mark the corresponding bifurcation points, and the solid line results from a linear regression based on the points between these two dashed lines.

stants τ are plotted versus the relative distance $\varepsilon=(\mathrm{Re}_i-\mathrm{Re}_{i,c})/\mathrm{Re}_{i,c}$ from the critical Reynolds number $\mathrm{Re}_{i,c}$ for $\mathrm{Re}_o=-156.0$ in Fig. 7 (○). A fit considering these experimental values results in $\tau\propto\varepsilon^{-0.994}$ and confirms the theoretical prediction of a supercritical Hopf bifurcation with $\tau\propto\varepsilon^{-1}$.

There is an obvious deviation in the linear relationship between $\langle v_{z,\min}\rangle^2$ and Re_i above $\mathrm{Re}_i=130.7$ depicted in Fig. 6(a) and marked by the second dashed line. Above that, Re_i on the amplitude grows stronger than the square root of SPI_+ (marked by the solid line) and a second frequency peak appears in the power spectrum as denoted in Fig. 6(b). This frequency corresponds to SWs (as shown in Fig. 1).

An axial scan of the flow state in this parameter regime is depicted in Fig. 8(a). It is recorded at $\mathrm{Re}_o=-156.0$ and $\mathrm{Re}_i=130.8$, which lies about $\Delta\mathrm{Re}_i=1.8$ above the axial scan shown in Fig. 2. In contrast to the axial scan at lower Re_i [Fig. 2(a), an oscillation cannot only be observed in the vicinity of the end plates, but also in the bulk of the system. In the corresponding power spectrum that is depicted in Fig. 8(d) the frequency peaks of SPI↑ and SPI↓ [marked by the green (light gray) and blue (dark gray) solid lines and indicated by (c) in the spectrum] are observed additionally to the ones *typical* for SPI_+ [marked by the two dashed lines and marked by (b) in the spectrum]. This is a strong indication for the coexistence of a SW and SPI_+ as exemplarily shown in Fig. 1.

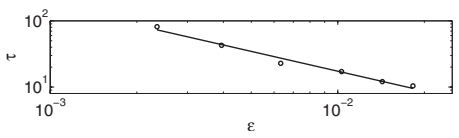

FIG. 7. Time constants τ versus ε determined at $\mathrm{Re}_o=-156.0$ at the axial position $h=19.8$ mm. The solid line is based on a fit with $\tau\propto\varepsilon^{-0.994}$.

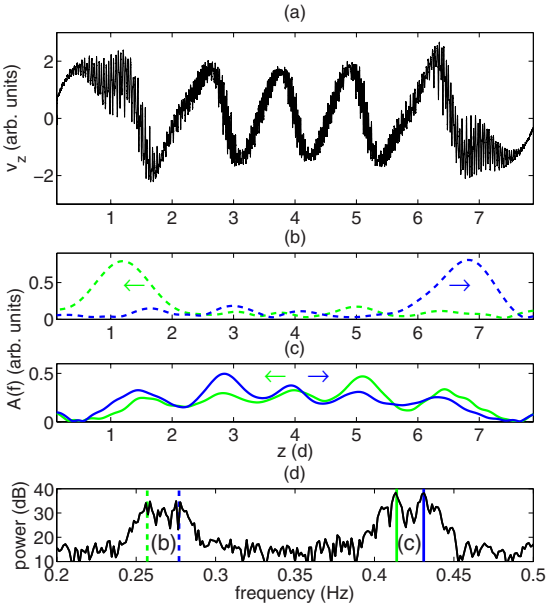

FIG. 8. (Color online) (a) Axial scan recorded at $\mathrm{Re}_o=-156.0$ and $\mathrm{Re}_i=130.8$, (b) amplitudes $A(f)$ of downward-directed SPI_+ [green (light gray) (0.246–0.266 Hz)] and upward-directed SPI_+ [blue (dark gray) dashed line (0.266–0.286 Hz)], (c) amplitudes $A(f)$ of SPI↓ [green (light gray) (0.402–0.422 Hz)] and SPI↑ [blue (dark gray) solid line (0.422–0.442 Hz)], and (d) power spectrum of (a). The [colored] dashed [solid] lines mark the corresponding frequencies in (b) [(c)].

The result of a bandpass-based analysis of the axial scan in Fig. 8(a) is depicted in (b) for the upward- and downward-propagating SPI_+. The amplitudes for these spirals are also estimated by the bandpass filtering—e.g., for the downward- [green (light gray), 0.246–0.266 Hz] and upward- [blue (dark gray) dashed line, 0.266–0.286 Hz] propagating SPI_+. The propagation directions of both SPI_+ are also indicated by two (colored) arrows.

In (c) the amplitudes, determined by a bandpass-based analysis, is shown for the oscillation frequencies of SPI↓ [green (light gray), 0.402–0.422 Hz] and SPI↑ [blue (dark gray) solid line, 0.422–0.442 Hz]. Additionally to the existence of nodal points in the axial scan (a) an almost uniform distribution of the spiral amplitude is visible. The nodal points are an important piece of evidence for the existence of SWs, which coexist with SPI_+ near the end plates.

The discrepancy between the linear regression and the square of the mean value of the minima $\langle v_{z,\min}\rangle^2$ above the second dashed line in Fig. 6(a) (marked with $\mathrm{SW}/\mathrm{SPI}_+$) is because of the appearance of SWs in the SPI_+ state. This is in contrast to the appearance of spiral vortices from SWs [14,21]. While in the latter case the spatial structure of the flow changes because of a steady bifurcation, the flow has still a single-oscillation frequency. Here, two different types of spiral modes with different oscillation frequencies and spatial amplitude distribution coexist.

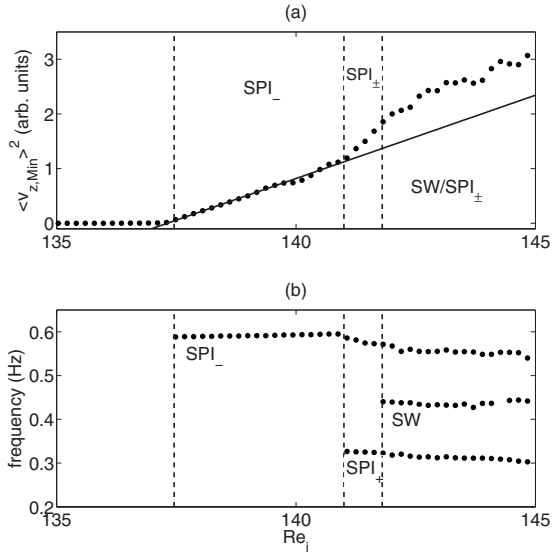

FIG. 9. Experimental bifurcation diagram recorded at $\mathrm{Re}_o=-200.0$ and axial position $h=28.2$ mm. (a) Square of the mean value of the oscillation minima $\langle v_{z,\min}\rangle^2$ and (b) corresponding oscillation frequencies versus Re_i for the SWs and the localized spirals SPI_+ and SPI_. The dashed lines mark the corresponding bifurcation points, and the solid line results from a linear regression based on the points between these two dashed lines.

D. Bifurcation behavior of SPI_

The transition from basic flow to localized spirals SPI_ is also characterized in the form of an experimental bifurcation diagram depicted in Fig. 9. As in Fig. 6 for the onset of SPI_+ the square of the mean value of the oscillation minima $\langle v_{z,\min}\rangle^2$ is plotted in Fig. 9(a) as an estimate for the square of the amplitude versus the control parameter Re_i. The measurements were performed for fixed $\mathrm{Re}_o=-200.0$ at an axial height of $h=28.2$ mm. Analog to Fig. 6 the corresponding oscillation frequencies of the flow states are depicted in Fig. 9(b).

At $\mathrm{Re}_{i,c}=137.4$ (marked by a vertical dashed line) SPI_ appears in basic laminar flow and the amplitude grows with Re_i by a square-root law. This can be seen from the linear fit to the squared amplitude performed between both vertical dashed lines in Fig. 9(a). Note that again an axial measurement position with zero axial velocity below the onset of SPI_ has been chosen. In addition to the square-root behavior of the amplitude the oscillation appears with a (finite) frequency corresponding to those of SPI_ (see Fig. 4) at $\mathrm{Re}_{i,c}$.

Analog to the corresponding experiments for SPI_+ also the transition to SPI_ is studied by performing a sudden small change in Re_i close to the onset of SPI_ in order to determine the time constants. The time constants τ are plotted versus the relative distance $\varepsilon=(\mathrm{Re}_i-\mathrm{Re}_{i,c})/\mathrm{Re}_{i,c}$ from the critical Reynolds number $\mathrm{Re}_{i,c}$ for $\mathrm{Re}_o=-200.0$ in Fig. 10 (○). A fit considering these experimental values results in $\tau\propto\varepsilon^{-0.878}$ and confirms the theoretical prediction of a supercritical Hopf bifurcation including a divergence of the time constants ($\tau\propto\varepsilon^{-1}$) as the control parameter approaches the critical point $\mathrm{Re}_{i,c}$.

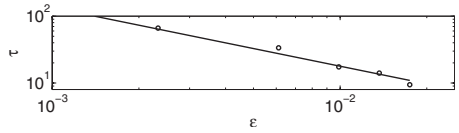

FIG. 10. Time constants τ versus ε determined at $\mathrm{Re}_o=-200.0$. The solid line is based on a fit with $\tau\propto\varepsilon^{-0.878}$.

Similar to SPI_+, as described in Sec. IV C, a more complicated flow occurs also from SPI_ at higher Re_i. This can be seen in Fig. 9(a) from the discrepancy of the linear fit (marked by a vertical dashed line) and in (b) from the appearance of additional frequency peaks corresponding to SPI_+ and to SWs (see Figs. 2 and 1, respectively) in the power spectrum. This provides evidence for the coexistence of SPI_ with SPI_+ (between the second and third dashed lines) and of SPI_, SPI_+, and SWs for higher Reynolds numbers (for Re_i above the third dashed line).

In Fig. 11(a) an axial scan of the axial velocity v_z recorded at $\mathrm{Re}_o=-200.0$ and $\mathrm{Re}_i=142.6$ is displayed. This is the region above the third dashed line in Fig. 9(b) where three different oscillation frequencies are detected. These three different *peaks* are also visible in the corresponding power spectrum depicted in (e), but as a result of the Doppler shift, each frequency peak has been split up into two peaks marked by the vertical dashed lines. The direction of axial

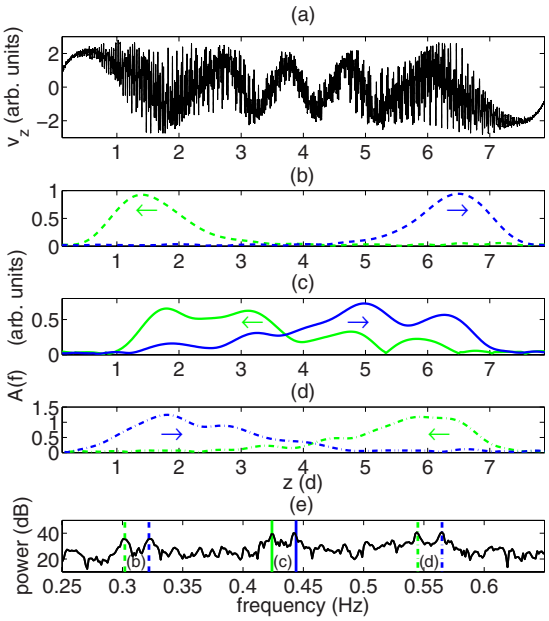

FIG. 11. (Color online) (a) Axial scan recorded at $\mathrm{Re}_o=-200.0$ and $\mathrm{Re}_i=142.6$, (b) amplitudes $A(f)$ of downward-propagating SPI_+ [green (light gray) (0.293–0.312 Hz)] and upward-propagating SPI_+ [blue (dark gray) dashed line (0.312–0.332 Hz)], (c) amplitudes $A(f)$ of SPI↓ [green (light gray) (0.415–0.435 Hz)] and SPI↑ [blue (dark gray) solid line (0.435–0.455 Hz)], (d) amplitudes $A(f)$ of downward-propagating SPI_ [green (light gray) (0.535–0.555 Hz)] and upward-propagating SPI_ [blue (dark gray) dash-dotted line (0.555–0.575 Hz)], and (e) power spectrum of (a). The dashed, solid, and dash-dotted lines mark the corresponding frequencies in (b), (c), and (d).

propagation of each traveling wave is additionally indicated by the small (colored) arrows in (b)–(d).

The double peak with the lowest frequencies in the power spectrum (e), indicated by the two dashed lines, corresponds to SPI_+. The amplitudes of both SPI_+ (determined by the bandpass-filtered axial scan) are depicted in (b)—e.g., green (light gray), downward-propagating SPI_+ (0.293–0.312 Hz); blue (dark gray) dashed line, upward-directed SPI_+ (0.312–0.332 Hz)—and marked by corresponding lines in (e). The typical oscillation frequency and axial amplitude distribution of traveling waves as for the *pure* SPI_+ state (see Fig. 2) can also be found in Figs. 11(e) and 11(b), respectively, for the mixed state.

The double peak with the highest frequencies in the power spectrum (e), indicated by the two dash-dotted lines, corresponds to SPI_. The amplitudes of SPI_ are depicted in Fig. 11(d)—e.g., green (light gray), downward-propagating SPI_ (0.535–0.555 Hz); blue (dark gray) dash-dotted line, upward-propagating SPI_ (0.555–0.575 Hz). As for SPI_+, also for SPI_, the typical oscillation frequency and axial amplitude profile with strong localizations near the end boundaries similar to those of a *pure* SPI_ state (see Fig. 4) is visible in the mixed state represented in Figs. 11(e) and 11(d), respectively.

The double peak in the middle of the power spectrum displayed in (e), indicated by the two solid lines, corresponds to the frequencies of the SWs (see Fig. 1). However, the amplitudes $A(f)$ depicted in (c)—e.g., green (light gray), SPI↓ (0.415–0.435 Hz); blue (dark gray) solid line, SPI↑ (0.435–0.455 Hz)—a difference in the axial amplitude distribution in the mixed state compared to those of a *pure* state is found (see Fig. 1). Each spiral has a preferred axial region—e.g., SPI↓ in the lower and SPI↑ in the upper parts of the system. Therefore the mixed state does not contain *pure* SWs, but localized spiral vortices in addition to the localized traveling waves of SPI_+ and SPI_.

E. Stability diagram of SWs, SPI_+, and SPI_

A stability diagram of SWs, SPI_+, and SPI_ is plotted in Fig. 12 where the inner and outer Reynolds numbers $(\mathrm{Re}_i, \mathrm{Re}_o)$ serve as control parameters. The numerically calculated linear instability of CCF with respect to $(m=\pm 1)$ spirals considering infinite axial length is represented by the dashed gray line. For $-145 \leq \mathrm{Re}_o \leq -120$ SWs (as marked in Fig. 12) appear from a supercritical Hopf bifurcation of the basic flow of the experimental system. These experimentally determined bifurcation points are in excellent agreement with the numerical calculations and confirm previous studies on SWs [24]. At higher Re_i these SWs disappear and Taylor vortex flow (TVF) becomes stable at the upper solid line. This transition from SWs to TVF shows a hysteresis that is indicated by the thin solid line in Fig. 12. Details of the bifurcation behavior of SWs can be found in [21,23,24].

For $\Gamma=8$ the region of SWs at higher Re_o is separated from the region of localized spirals at lower Re_o by a gap in the vicinity of $\mathrm{Re}_o=-147(\pm 2)$. There, continuous transitions from basic flow to TVF occur. Below $\mathrm{Re}_o=-150$ the bifurcation behavior of the flow changes completely: A supercritical Hopf bifurcation from basic flow to SPI_+ occurs as exemplarily shown for $\mathrm{Re}_o=-156.0$ in Fig. 6. The measured bifurcation points (dash-dotted line) confine the region of oscillatory flow (marked by SPI_+) at lower but also at higher Re_i where a transition from SPI_+ to steady TVF occurs by increasing Re_i. The onset of SPI_+ at lower Re_i in the basic laminar flow occurs below the linear instability threshold of CCF toward spiral vortices in systems of infinite axial length.

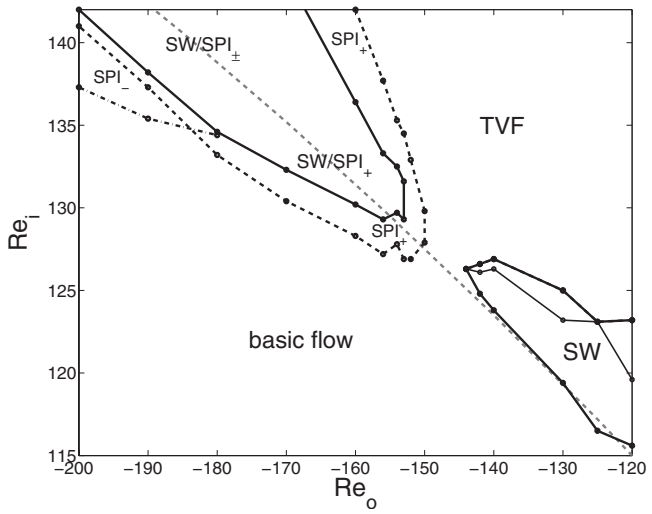

FIG. 12. Stability diagram for $\Gamma=8$. The dashed gray line represents linear instability of CCF with respect to $m=\pm 1$ spirals considering infinite axial length. SWs appear very close to the linear instability of CCF while the onset of SPI_+ (dashed line) and SPI_ (dash-dotted line) is significantly below. The region of coexistent localized spirals at the end boundaries and in the bulk is marked with $\mathrm{SW/SPI}_\pm$. At higher Re_i steady Taylor vortices (TVF) appear from SWs at higher and from SPI_+ at lower Re_o.

Encapsulated within the SPI_+ region there is a region of coexistence of SWs and SPI_+ for $\mathrm{Re}_o>-180$ (denoted with $\mathrm{SW/SPI}_+$), and SWs and $SPI_\pm$ for $\mathrm{Re}_o<-180$ denoted with $\mathrm{SW/SPI}_\pm$ are marked with a solid line. The localized structures of the flow—e.g., SPI_+ and SPI_—coexist with SWs in the bulk of the system (as exemplarily shown in Figs. 8 and 11). The border of this region is determined from the discrepancy to the square-root behavior of the amplitude of SPI_+, as presented above for $\mathrm{Re}_o=-156$ in Fig. 6.

Below $\mathrm{Re}_o=-185$ SPI_ appears in the basic laminar state from a supercritical Hopf bifurcation (dash-dotted line) denoted in Fig. 12 by SPI_. A region of coexistence of SPI_ and SPI_+ as well as of SPI_, SPI_+, and SWs appears at higher Re_i such as presented for $\mathrm{Re}_o=-200$ in Fig. 9.

F. Oscillation frequencies

In Fig. 13 the oscillation frequencies of the SWs (solid line), SPI_+ (dashed line), and SPI_ (dash-dotted line) are displayed versus Re_o. Additionally the frequencies resulting from linear stability analysis are plotted as the dashed gray line.

For $-180 \leq \mathrm{Re}_o \leq -120$ a reasonable agreement (approximately 2%) between the numerical and experimental fre-

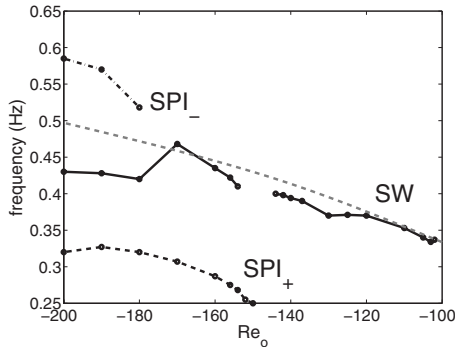

FIG. 13. Oscillation frequencies of the SWs (solid line), SPI_+ (dashed line), and SPI_ (dash-dotted line) versus Re_o. The dashed gray line represents the oscillation frequencies from the linear stability analysis for $m=\pm 1$.

quencies of the SWs can be found (no oscillatory state appears in the vicinity of $Re_o=-147$). The agreement is excellent for higher $Re_o \approx -110$, but decreases for lower Re_o. Note that below $Re_o=-150$ SWs do not occur as primary flow anymore. Below $Re_o=-180$ this discrepancy further increases up to 14%. This Re_o corresponds to the onset of SPI_ additionally to SPI_+. The frequency of SPI_+ is measured in the region of $Re_o \leq -150$ and lies always below the numerically calculated one. In contrast to that the oscillation frequency of SPI_ is systematically larger (approximately 15%) than this frequency and has been detected below $Re_o=-180$. The frequencies of SPI_+ and SPI_ differ significantly from the spiral frequency determined from linear stability analysis of circular Couette flow considering an infinite axial length.

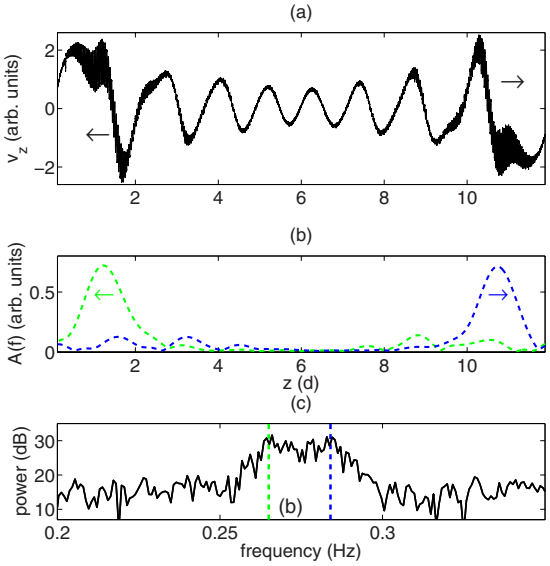

FIG. 14. (Color online) (a) Axial scan of SPI_+ recorded at $\Gamma=12$, $Re_o=-155.0$, and $Re_i=128.8$, (b) amplitudes $A(f)$ of downward-propagating SPI_+ [green (light gray) (0.255–0.275 Hz)] and upward-directed SPI_+ [blue (dark gray) dashed line (0.275–0.295 Hz)], and (c) power spectrum of (a). The dashed lines mark the corresponding frequencies in (b).

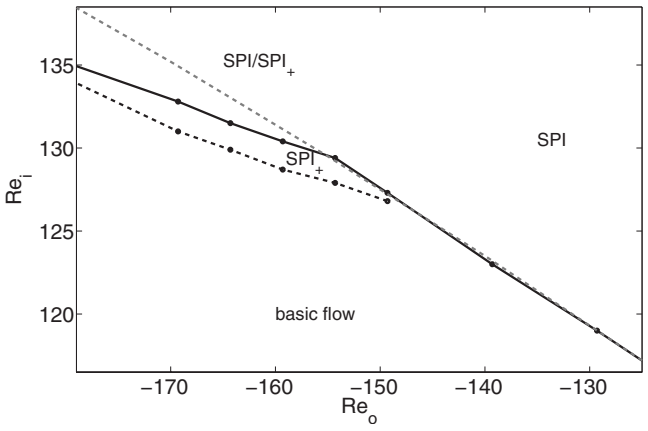

FIG. 15. Stability diagram for $\Gamma=12$. The dashed gray line represents the linear instability of CCF with respect to $m=\pm 1$ spirals considering infinite axial length. SPIs appear very close to linear instability in the (basic flow) while the onset of SPI_+ (dashed line) is significantly below. The region of coexistent localized spirals at the end boundaries and in the bulk is marked with SPI/SPI_+. At higher Re_i steady Taylor vortices (TVF) appear from SWs at higher and from SPI_+ at lower Re_o.

G. Localized spirals in larger-aspect-ratio systems

The existence of this type of localized spiral vortices ($SPI_\pm$) is not limited to an aspect ratio $\Gamma=8$ as studied in detail in the previous sections. An example of localized spirals in systems with a larger aspect ratio is given in Fig. 14. In (a) an axial scan of SPI_+ recorded in a system with $\Gamma=12$ for $Re_o=-155.0$ and $Re_i=128.8$—e.g., for very similar Reynolds numbers as the measurement of SPI_ at $\Gamma=8$—is shown in Fig. 2. The strongly localized amplitude close to the end plates which is typical for SPI_+ can be seen in the amplitude distribution depicted in Fig. 14(b). This is obtained from bandpass filtering of the power spectrum (c) with frequency bands around the peaks (marked by vertical dashed lines). These peaks correspond to the typical (Doppler-shifted) frequency of SPI_+ which is below the spiral frequency as already found for $\Gamma=8$ (see Figs. 8 and 13).

In Fig. 15 a stability diagram for $\Gamma=12$ is depicted. The dashed gray line represents values from linear instability of CCF with respect to $m=\pm 1$ spirals considering an infinite axial length.

The experimentally determined onset of spiral vortex flow (SPI) is close to that linear instability of CCF for smaller

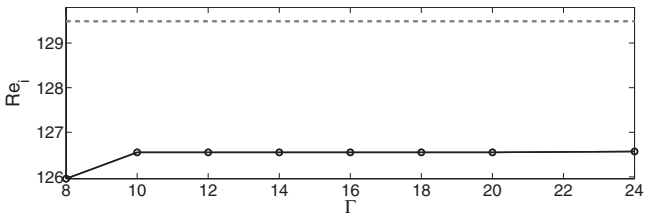

FIG. 16. Onset of SPI_+ versus the aspect ratio Γ [(○) black solid line]. The dashed gray line corresponds to the linear instability threshold of CCF with respect to $m=\pm 1$ spirals.

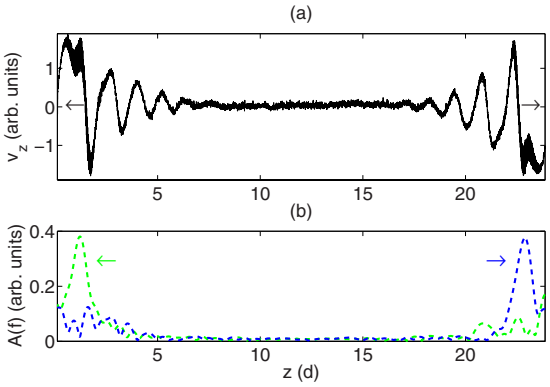

FIG. 17. (Color online) (a) Axial scan of SPI_+ recorded at $\Gamma=24$, $Re_o=-156.0$, and $Re_i=130.2$ and (b) amplitudes $A(f)$ of downward-propagating SPI_+ [green (light gray) (0.255–0.275 Hz)] and upward-directed SPI_+ [blue (dark gray) dashed line (0.275–0.295 Hz)].

counterrotation $Re_o > -150$. It can be seen that the onset of SPI_+ (dashed black line) is significantly below the linear instability of CCF (dashed gray line). The region of coexistent localized spirals at the ends and spirals in the bulk is marked with SPI/SPI_+. Note that even the onset of the spirals in this parameter regime is systematically below the linear instability of CCF.

In order to study the dependence of the appearance of the localized spirals with respect to the aspect ratio, the onset of SPI_+ is plotted in Fig. 16 versus the aspect ratio Γ [(○), black solid line] for $Re_o=-156.0$. In addition to these experimentally determined values also the linear instability threshold of CCF with respect to $m=\pm 1$ spirals is plotted as the dashed gray line. One can see that the onset of SPI_+ lies systematically below the linear instability of CCF and is almost independent from Γ.

In Taylor-Couette flow with larger aspect ratios Γ the Ekman-induced vortex structure is not yet fully developed in the bulk of the system. An example of the SPI_+-state at larger Γ represented by an axial scan is depicted in Fig. 17. The measurement is recorded at $Re_o=-156$, $Re_i=130.2$, and $\Gamma=24$. They have been measured in the same Reynolds number regime as for $\Gamma=8$ and $\Gamma=12$—i.e., also below the linear instability of CCF. The oscillation in this axial scan is also located at the ends, and the oscillation frequencies that have been detected at these positions are found to be identical to those at lower aspect ratios.

In addition to these axial scans a flow visualization measurement of the localized spirals SPI_ is performed. As mentioned in Sec. IV B these spirals are right handed in the upper and left handed in the lower parts of the system and are axially traveling toward the middle of the system and this behavior can also be seen in the flow visualization photographs depicted in Fig. 18. Furthermore, it is clearly visible that the spiral structure appears in a small layer close to the inner cylinder.

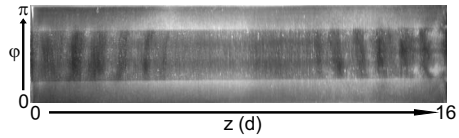

FIG. 18. Flow visualization of the localized spirals SPI_ recorded at $\Gamma=16$, $Re_o=-200.0$, and $Re_i=140.0$.

V. CONCLUSIONS

We reported on an experimental and numerical investigation on a type of localized spirals (SPI_+ and SPI_) in counterrotating Taylor-Couette flow. These spirals both travel in the axial direction and propagate either to the end plates (SPI_+) or to the axial middle (SPI_). They appear from a supercritical Hopf bifurcation for sufficiently high rates of counterrotation—e.g., for $Re_o \lesssim -150$ at $\eta=0.5$—in the basic laminar flow of a Taylor-Couette system with rigid end plates at bottom and top. Their critical point is below the numerically determined linear instability of circular Couette flow—e.g., for a system of infinite axial length—where spiral vortices typically appear from a Hopf bifurcation with O(2) symmetry.

Both these spiral states—e.g., SPI_+ and SPI_—differ significantly in their axial amplitude profile, oscillation frequency, and symmetry from spiral vortices and except for the latter point also from standing waves. The oscillation of both states $SPI_\pm$ occurs strongly localized near each end boundary almost independently from the aspect ratio, and their oscillation frequency is significantly below (SPI_+) or above (SPI_) the spiral frequencies that occur at the linear instability of circular Couette flow. Both states keep either a spatial (SPI_+) or a spatiotemporal (SPI_) reflection symmetry which is typically broken at the onset of spiral vortices. Only standing waves keep those symmetries, but also differ significantly in amplitude profile and oscillation frequency from $SPI_\pm$. These states are not replaced by spirals or standing waves, respectively, at higher inner Reynolds number, but they can coexist and form flow states which consist of two [SPI(SW)/SPI_] or three different [$SPI(SW)/SPI_\pm$] types of traveling waves.

Therefore we conclude that the spiral states SPI_+ and SPI_ are a type of nonaxisymmetric solution of counterrotating Taylor-Couette flow. These flow states are ultimately related to the inhomogeneous basic flow in Taylor-Couette systems with rigid boundaries since they are not captured by the linear instability of circular Couette flow. Furthermore, we found that the appearance of these spiral states does not depend on the aspect ratio.

ACKNOWLEDGMENT

We acknowledge support from the Deutsche Forschungsgemeinschaft.

[1] R. C. DiPrima and H. L. Swinney, *Instabilities and Transition in Flow between Concentric Cylinders* (Springer-Verlag, New York, 1981), p. 139.
[2] J. Guckenheimer and P. Holmes, *Nonlinear Oscillations, Dynamical Systems and Bifurcations of Vector Fields* (Springer-Verlag, New York, 1986).
[3] M. C. Cross and P. C. Hohenberg, Rev. Mod. Phys. **65**, 851 (1993).
[4] R. Tagg, Nonlinear Sci. Today **4**(3), 2 (1994).
[5] C. Egbers and G. Pfister, *Physics of Rotating Fluids* (Springer-Verlag, Berlin, 2000).
[6] P. Chossat and G. Iooss, *The Couette-Taylor Problem* (Springer-Verlag, Berlin, 1994).
[7] M. Golubitsky and I. Stewart, SIAM J. Math. Anal. **17**, 249 (1986).
[8] M. Golubitsky and W. F. Langford, Physica D **32**, 362 (1988).
[9] W. F. Langford, R. Tagg, E. J. Kostelich, H. L. Swinney, and M. Golubitzky, Phys. Fluids **31**, 776 (1988).
[10] E. R. Krueger, A. Gross, and R. C. di Prima, J. Fluid Mech. **24**, 521 (1966).
[11] H. A. Snyder, Phys. Fluids **11**, 728 (1968).
[12] C. D. Andereck, S. S. Lui, and H. L. Swinney, J. Fluid Mech. **164**, 155 (1986).
[13] J. Sanchez, D. Crespo, and F. Marques, Appl. Sci. Res. **51**, 55 (1993).
[14] C. Hoffmann and M. Lücke, *Physics of Rotating Fluids* (Springer-Verlag, Berlin, 2000), pp. 55–66.
[15] T. B. Benjamin, Proc. R. Soc. London, Ser. A **359**, 1 (1978).
[16] T. B. Benjamin, Proc. R. Soc. London, Ser. A **359**, 27 (1978).
[17] T. B. Benjamin and T. Mullin, Proc. R. Soc. London, Ser. A **377**, 221 (1981).
[18] C. Hoffmann, M. Lücke, and A. Pinter, Phys. Rev. E **72**, 056311 (2005).
[19] J. D. Crawford and E. Knobloch, Nonlinearity **1**, 617 (1988).
[20] A. S. Landsberg and E. Knobloch, Phys. Rev. E **53**, 3579 (1996).
[21] J. Langenberg, G. Pfister, and J. Abshagen, Phys. Rev. E **68**, 056308 (2003).
[22] C. Hoffmann, M. Lücke, and A. Pinter, Phys. Rev. E **69**, 056309 (2004).
[23] J. Langenberg, G. Pfister, and J. Abshagen, Phys. Rev. E **70**, 046209 (2004).
[24] J. Langenberg, G. Pfister, and J. Abshagen, Phys. Fluids **16**, 2757 (2004).
[25] J. Abshagen, J. Langenberg, G. Pfister, T. Mullin, S. J. Tavener, and K. A. Cliffe, Theor. Comput. Fluid Dyn. **18**, 129 (2004).
[26] G. Pfister and U. Gerdts, Phys. Lett. **83A**, 23 (1981).
[27] B. Hof and T. Mullin, Magnetohydrodynamics **37**, 119 (2001).
[28] J. Abshagen, O. Meincke, G. Pfister, K. A. Cliffe, and T. Mullin, J. Fluid Mech. **476**, 335 (2003).